Infinite Science
Publishing

Research Article

Single-Sided Hybrid Selection Coils for Field-Free Line Magnetic Particle Imaging

Alexey Tonyushkin*

Physics Department, University of Massachusetts Boston, Boston, MA, USA
*Corresponding author, email: alexey.tonyushkin@umb.edu

Abstract

Single-sided Magnetic Particle Imaging (MPI) is a promising new development that can help translating MPI technology into clinical practice. Unlike currently available closed geometry MPI scanners, single-sided devices do not have any hardware around the object. The major progress includes a demonstration of 2D imaging on a single-sided device that utilizes a field-free point coplanar coil topology. Previously, we proposed a design of a field-free line selection field generator for a single-sided geometry. Here, we extend our single-sided design to incorporate a much more efficient scheme that utilizes permanent magnets.

I. Introduction

Magnetic Particle Imaging (MPI) [1, 2] is a promising imaging modality that has potential to outperform other imaging techniques. In order to show the feasibility in a clinical scenario, MPI needs to be scaled. The major challenge of such an upscaling is the high power consumption of the system. Additionally, there are constraints on the size of FOV due to physiological stimulation and specific absorption rate associated with large switching fields [3, 4]. A complimentary MPI topology approach is designing a single-sided or asymmetric MPI device that does not inclose large FOVs but instead acts as a surface probe [5]. Although such device may have penetration limits it can be effective for cancer screening [6] as well as for susseptometry. To date a working prototype of a single sided MPI scanner utilizes a field-free point (FFP) geometry of the selection field [7]. While it shows promising results [8–10] the major issue of small signal to noise still remains. An alternative MPI method utilizes a so called field-free line (FFL) [11–13] that offers larger signal to noise and can be faster than FFP MPI. Previously, an FFL single-sided MPI geometry with elongated elec-

tromagnets capable of multidimensional encoding was suggested [14].

In this paper we offer an effective modification of the previous FFL design that incorporates four permanent magnets, which form the basis of the static selection field. The presented simulation study shows that such a device can be used for multidimensional image encoding, while cutting down the power consumption and relaxing cooling requirements.

II. Theory and Methods

II.I. FFL generator magnet design

The static selection coils consist of four parallel blocks of vertically polled permanent magnets that are shown in Fig. 1. The blocks are arranged into inner and outer pairs with the magnetization magnitudes M_1 and M_2 respectively. We consider surface magnetization to be equal to magnetization remanence. To fulfill the zero field condition the magnetization vector of each adjacent magnet has to be antiparallel to each other and $M_1 <$
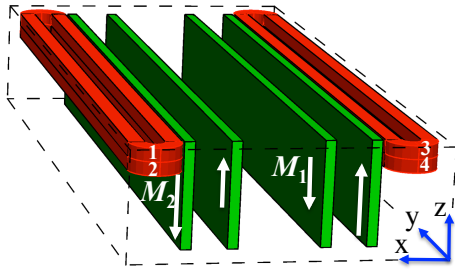
Figure 1: A schematic diagram of single-sided hybrid selection coils for FFL MPI. The FFL is generated by four permanent magnets along the y-axis above the coils. Their magnetizations are given by $\vec{M}_1$ for the inner pair and $\vec{M}_2$ for the outer pair (white arrows). The two pairs of elongated electromagnets (1,3 and 2,4) can dynamically shift the FFL along the x-axis or z-axis. The setup can be mechanically rotated around the z-axis enabling in-plane projection encoding.

M_2. Such configuration of the magnetizations creates two competing magnetic fields $\vec{H}_1$ and $\vec{H}_2$, which are oriented along x-axis and opposite to each other at the isoplane. The FFL is generated along y-axis at $z = h$ for $\vec{H}_1(h) = -\vec{H}_2(h)$. The schematic plots of the magnetic fields from the inner and outer pairs of magnets and the superposition field and a vector plot of the resulting magnetic field are shown in Fig. 2(a,b) respectively.

The choices of the magnetizations of the permanent magnets and the geometry such as the gaps between each pair define the property of resulting FFL, i.e. its height and the gradient strength. The ideal field with strong gradient is created by closely positioned two inner magnets that generates rapid field decay along z-axis and widely separated strong outer magnets that generate quasi-uniform field (see Fig. 2(a)). In practice, the geometry is constrained by the dimensions of the blocks and coils, although the mechanical adjustment of the gaps can be incorporated into the actual device. The choice of the surface magnetizations at the fixed geometry defines the magnetic field properties, so that the base height of FFL is reciprocal to the ratio of magnetizations $m = M_2/M_1$, i.e. for $m = 1, h \rightarrow \infty$, for $m \gg 1, h \rightarrow 0$. The gradient strength is proportional to the magnitude of the magnetizations, so for fixed m the gradient doubles if both magnetizations double, while the height stays constant. For example, if the gaps between the inner and outer magnets are 14.5 mm and 87 mm respectively, $M_1 = 0.6/4\pi \, \mathrm{T}\mu_0^{-1}$, $M_2 = 2/4\pi \, \mathrm{T}\mu_0^{-1}$ then the gradient $G = 7 \, \mathrm{T/m}$ at the height $h = 10 \, \mathrm{mm}$.

II.II. Hybrid drive-selection coil design for image encoding

The described design of the selection coil based on all permanent magnets can in principle be used with mechanical motion in a similar fashion to [15] or in combi-

nation with the external drive field coils. Here we present an all-in-one concept of the coils that are self-sufficient for 3-D image encoding.

To offset the magnetic field from the permanent magnets we consider two sets of elongated coils [16] outside of the outer pair of the permanent magnets as shown in Fig. 1. The two sets of coils can be used independently from each other displacing the FFL with arbitrary pattern across the xz-plane.

The bias magnetic field from the outer electromagnet coils (2,4) with out-of-phase mutual current pattern shifts the FFL in the yz-plane. These coils can be used as z-drive coils with AC current:

$$I_z(t) = I_0^z \sin(2\pi f_z t), \tag{1}$$

where I_0^z is the current amplitude that defines the depth encoding, $f_z = 10-25 \, \mathrm{kHz}$ is the drive frequency.

For 3-D image encoding a second pair of coils is required to displace the FFL along the x-axis. In our model design these x-drive pair of coils (1,3) are placed on top of z-drive coils as shown in Fig. 1. The two x-coils are driven with in-phase mutual AC current:

$$I_x(t) = I_0^x \sin(2\pi f_x t), \tag{2}$$

where I_0^x is the current amplitude that defines Δx encoding, $f_x = 10-25 \, \mathrm{kHz}$ is the drive frequency. With the appropriately chosen parameters and dimensions of the coils the FFL can be oscillated along x-axis. Therefore, 3-D image encoding can be done by independently driving x- and z-coils with AC current and simultaneous rotation of the device around the z-axis for projection reconstruction [17, 18].

III. Simulation results

To study the magnetic field generated by the permanent magnets and electromagnetic coils we carried out quasi-static simulations using Wolfram *Mathematica*® software with *Radia* package (ESRF France). The package allows calculating the magnetic flux density $\vec{B}$ (here, we call it B-field) from a set of magnetized blocks and coils with DC currents by utilizing boundary Integral Methods and requires much less computational power than analogous FEM based simulations [19].

First let us consider a static FFL generated by a permanent magnet arrangement as described in Section II.I. For simplicity, in our proof-of-principle simulation model we choose all four magnets with equal dimensions: length $l = 300 \, \mathrm{mm}$, width $w = 50 \, \mathrm{mm}$, and thickness $t = 5 \, \mathrm{mm}$. We set the inner and outer magnets' separations to be $\Delta_1 = 34.5 \, \mathrm{mm}$ and $\Delta_1 = 69 \, \mathrm{mm}$ respectively, and the magnetizations: $M_1 = 0.5/4\pi \, \mathrm{T}\mu_0^{-1}$, $M_2 = 1/4\pi \, \mathrm{T}\mu_0^{-1}$ so that $m = 2$. Figure 3 shows simulations of the magnetic field B from the complete set of permanent magnets defined
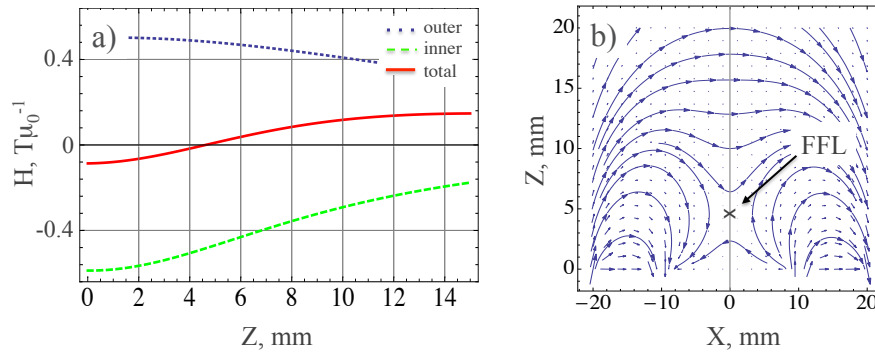
Figure 2: Static selection magnetic field along the z-axis at $x = 0$ generated by the the inner (green dashed-line), the outer (blue dotted-line) sets of magnets, and their superposition (red thick-line) (a); vector plot of the total magnetic field in the xz-plane showing a formation of an FFL (b).
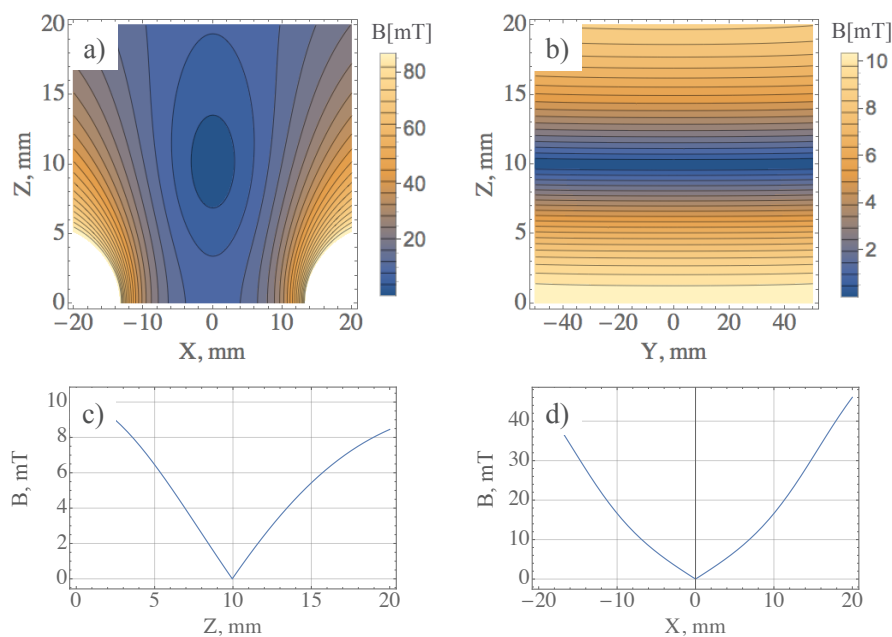
Figure 3: Static field of the selection coils made out of four permanent magnets with the FFL generated at $z = 10$ mm above the surface. Simulated magnetic field B contour plots in the xz-plane (a) and the yz-plane (b); B-field magnitude plots along the z-axis at $x = 0$ (c), and the x-axis at $z = 10$ mm (d).
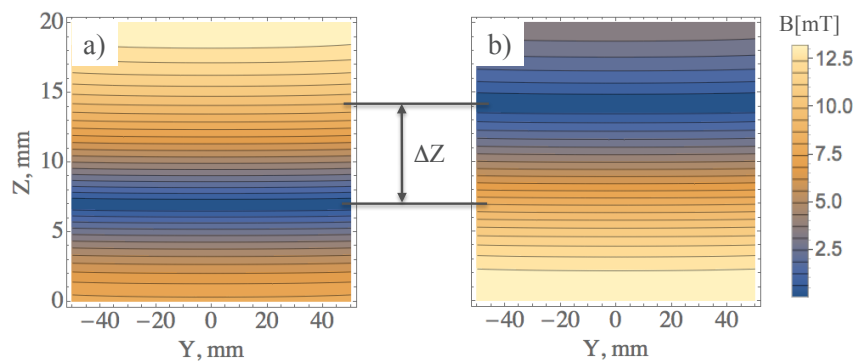
Figure 4: Z-axis encoding with the single-sided MPI device: magnetic field contour plots in the yz-plane show the FFL at (a) $z = 7$ mm for $I_z(t) = -100$ A and (b) $z = 14$ mm for $I_z(t) = 100$ A above the surface, respectively.
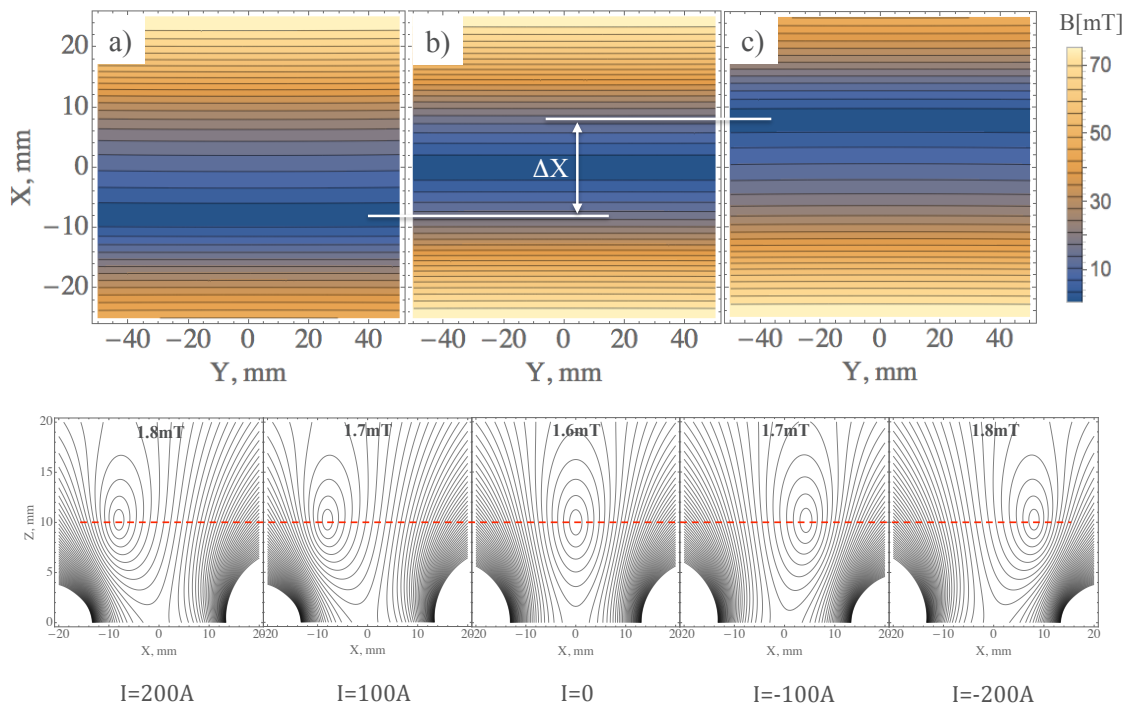
Figure 5: X-axis encoding in the *xy*-plane: the top row - magnetic field contour plots with the FFL at (a) $x = -8$ mm for $I_x(t) = 200$ A, (b) $x = 0$ mm for $I_x(t) = 0$ A, and (c) $x = 8$ mm for $I_x(t) = -200$ A, respectively, showing the FFL spans for $\Delta x = 16$ mm; the bottom row - *xz*-plane contour plots show a linear FFL trajectory $x(I_x(t))$ with constant $z = 10$ mm, as shown by a red dashed-line; the contour lines separations are indicated for each plot in the bottom row.

above. The contour plots (Fig. 3(a,b)) show the quality of the generated magnetic field and FFL at the height of $h = 10$ mm above the surface of the magnets. The magnetic field magnitude plots along *z*-axis and *x*-axis (Fig. 3(c,d)) show the respective gradients of the field with the maximum strength $G = 1.2$ T/m. The specified geometry provides a flat FFL over the $(-50 < y < 50)$ mm region that depends on the aspect ratio of the magnets.

The image encoding in our coils assembly design is performed by means of symmetrically located elongated electromagnetic coils as shown in Fig. 1. The top set of the coils denoted as (1,3) are used as x-drive coils and the bottom pair (2,4) are used as z-drive coils. In our quasi-static simulations we concentrate on the proof-of-principle magnet generator for static shifting of an FFL and thus use a certain electromagnet design that utilizes a plane conductor. Each simulated electromagnet has the following dimensions: straight length $l = 300$ mm, width $w = 24$ mm, height $h = 6.4$ mm, and core width $s = 9$ mm. The model conductor is made of $N = 25$ windings of conducting tape with the crosssection: 6.33×0.3 mm^2.

The simulations results for the magnetic field of the selection coils operated in combination with z-drive (2,4) coils are shown in Fig. 4. The instantaneous currents $I_z(t) = -100$ A and $I_z(t) = 100$ A (see Eq. 1) shift the FFL to $z = 7$ mm and $z = 14$ mm above the surface respectively. Thus, the peak current of 100 A allows en-

coding $\Delta Z = 7$ mm. The gradient strength, however, does not stay constant over the depth span, which is inherent drawback of single-sided devices. So for the low trajectory point $G = 1.5$ T/m and for the upper point $G = 0.9$ T/m. This difference of gradient strength has to be taken into the account and corrected for at the image reconstruction stage.

Figure 5 shows the simulations results from the operation of the selection coils in combination with the x-drive (1,3) electromagnetic coils. The FFL displacement in *xy*-plane is shown in the top row of Fig. 5(a-c), where the FFL oscillates from (a) $x = -8$ mm for $I_x(t) = 200$ A to (b) $x = 0$ mm for $I_x(t) = 0$ A, and (c) $x = 8$ mm for $I_x(t) = -200$ A, respectively, showing overall image encoding along *x*-axis over $\Delta X = 16$ mm. The bottom row of Fig. 5 shows the FFL trajectory $x(I_x(t))$, while the height above the surface stays constant at $z = 10$ mm. The z-drive coils can be operated at the same time allowing *xz*-plane encoding.

The above simulations show an example of *xz*-plane FOV encoding of 16×7 mm^2 that can be linearly upscaled with corresponding higher peak currents. The actual MPI device would benefit from the higher gradient strength that can be obtained for permanent magnets with larger surface magnetizations (see Sec. II.I), although, to encode the same FOV it would also require higher peak currents in both sets of drive coils.

IV. Discussion

The presented simulations of a model selection-drive system consisting of hybrid coils prove feasibility for 3-D imaging for an MPI device. However, the challenge of any single-sided geometry is in decreasing gradient strength and inhomogeneity of the magnetic field along the z-axis that results in variable spatial resolution and also makes it difficult to apply robust x-space image reconstruction method. Alternatively, such an MPI device can be used for 2-D imaging in the xy-plane with slice selection along the z-axis, where the in-plane image reconstruction can be fast and robust.

The geometry with several pairs of elctro- and permanent magnets that are arranged symmetrically from the isoplane can potentially generate multiple field zero lines when driven with high peak current. The spurious signal from magnetic particles located in the secondary FFL, which is outside of the FOV, can be eliminated with proper choice of the receive sensitivity matrix. Such a receive profile can be created by the elongated receive coils that are placed above and in parallel with the respective drive coils with their dimensions defining the in-plane FOV.

The single-sided MPI device can be constructed from the hybrid coils with the above specified parameters. The actual electromagnet design, which is rated for 2.5 kW DC power consumption, can be adopted from [16]. The rare-earth permanent magnets can be compounded to provide the required size and the field strength. Although, the specified length of the permanent magnets provide over 8 cm long linear FFL, reducing the coil's length by half still produces a tolerable curvature of the FFL in the 4 cm long range [14].

The simulation results of the x-drive operation show a linear FFL trajectory along the x-axis with the constant height (the bottom row of Fig. 5), which is a feature of the presented magnet topology. However, some coil topologies, such as all-electromagnet coils, may create a shift of FFL height at the edges of FOV. In this case, the trajectory can be corrected by modulating the z-drive coils with a relatively low current thus offsetting the static height.

The practical dimensions and the choice of the magnet strengths and the driving peak currents have to be defined by the specific application rather than made universal. As such the exact power consumption would depend on the optimizations of the parameters of the conductors and magnet properties. For example, an in-plane imaging with submillimeter resolution requires gradients of ~ 10 T/m that can be provided with strong magnets.

Finally, an alternative hybrid coils design can be created with the electromagnets located between the inner and the outer sets of permanent magnets, which can reduce drive current, however, the FFL from such a coil arrangement is less stable with regards to generation of a secondary FFL. In future work we plan to perform a feasibility study of scaling the single-sided device to enclose larger FOV, while optimizing the power consumption.

V. Conclusions

We presented a simulation based feasibility study of a novel design of a single-sided FFL-based selection coils with permanent magnets, which is capable of multidimensional imaging. An MPI device based on the selection coils can provide a strong magnetic field gradient with a relatively flat FFL and large FOV within the physiological safety operation limit. With sufficient peak current FFL can encode the whole volume of a small animal or penetrate into peripheral human organs.

Acknowledgment

References

[1] B. Gleich and J. Weizenecker. Tomographic imaging using the nonlinear response of magnetic particles. *Nature*, 435(7046):1214–1217, 2005. doi:10.1038/nature03808.

[2] T. Knopp and T. M. Buzug. *Magnetic Particle Imaging: An Introduction to Imaging Principles and Scanner Instrumentation.* Springer, Berlin/Heidelberg, 2012. doi:10.1007/978-3-642-04199-0.

[3] O. Doessel and J. Bohnert. Safety considerations for magnetic fields of 10 mT to 100 mT amplitude in the frequency range of 10 kHz to 100 kHz for magnetic particle imaging. *Biomed. Tech. / Biomed. Eng.*, 58(6):611–621, 2013. doi:10.1515/bmt-2013-0065.

[4] I. Schmale, B. Gleich, J. Rahmer, C. Bontus, J. Schmidt, and J. Borgert. MPI Safety in the View of MRI Safety Standards. *IEEE Trans. Magn.*, 51(2):6502604, 2015. doi:10.1109/TMAG.2014.2322940.

[5] T. F. Sattel, T. Knopp, S. Biederer, B. Gleich, J. Weizenecker, J. Borgert, and T. M. Buzug. Single-sided device for magnetic particle imaging. *J. Phys. D: Appl. Phys.*, 42(1):1–5, 2009. doi:10.1088/0022-3727/42/2/022001.

[6] K. Gräfe, T. F. Sattel, K. Lüdtke-Buzug, D. Finas, J. Borgert, and T. M. Buzug. Magnetic-Particle-Imaging for Sentinel Lymph Node Biopsy in Breast Cancer. In *Springer Proceedings in Physics*, volume 140, pages 237–241, 2012. doi:10.1007/978-3-642-24133-8_38.

[7] K. Gräfe, M. Grüttner, T. F. Sattel, M. Graeser, and T. M. Buzug. Single-sided magnetic particle imaging: Magnetic field and gradient. In *SPIE Medical Imaging*, 2013. doi:10.1117/12.2001610.

[8] K. Gräfe, G. Bringout, M. Graeser, T. F. Sattel, and T. M. Buzug. System Matrix Recording and Phantom Measurements with a Single-Sided Magnetic Particle Imaging Device. *IEEE Trans. Magn.*, 51 (2):6502303, 2015. doi:10.1109/TMAG.2014.2330371.

[9] C. Kaethner, M. Ahlborg, K. Gräfe, G. Bringout, T. F. Sattel, and T. M. Buzug. Asymmetric Scanner Design for Interventional Scenarios in Magnetic Particle Imaging. *IEEE Trans. Magn.*, 51(2):6501904, 2015. doi:10.1109/TMAG.2014.2337931.

[10] K. Gräfe, A. von Gladiss, G. Bringout, M. Ahlborg, and T. M. Buzug. 2D Images Recorded With a Single-Sided Magnetic Particle Imaging Scanner. *IEEE Trans. Med. Imag.*, 35(4):1056–1065, 2016. doi:10.1109/TMI.2015.2507187.

[11] J. Weizenecker, B. Gleich, and J. Borgert. Magnetic particle imaging using a field free line. *J. Phys. D: Appl. Phys.*, 41(10):105009, 2008. doi:10.1088/0022-3727/41/10/105009.

[12] T. Knopp, M. Erbe, S. Biederer, T. F. Sattel, and T. M. Buzug. Efficient generation of a magnetic field-free line. *Med. Phys.*, 37(7): 3538–3540, 2010. doi:10.1118/1.3447726.

[13] T. Knopp, T. F. Sattel, S. Biederer, and T. M. Buzug. Field-free line formation in a magnetic field. *J. Phys. A,* 43(1):012002, 2010. doi:10.1088/1751-8113/43/1/012002.

[14] A. Tonyushkin. Single-sided FFL-based MPI device with depth encoding. In *International Workshop on Magnetic Particle Imaging*, 2016.

[15] H. Bagheri, C. A. Kierans, K. J. Nelson, B. A. Andrade, C. L. Wong, A. L. Fredrick, and M. E. Hayden. A novel scanner architecture for MPI. In *International Workshop on Magnetic Particle Imaging*,

2015. doi:10.1109/IWMPI.2015.7107089.

[16] A. Tonyushkin and M. Prentiss. Straight macroscopic magnetic guide for cold atom interferometer. *J. Appl. Phys*, 108(9):094904, 2010. doi:10.1063/1.3506685.

[17] P. W. Goodwill, J. J. Konkle, B. Zheng, E. U. Saritas, and S. M. Conolly. Projection X-Space Magnetic Particle Imaging. *IEEE Trans. Med. Imag.*, 31(5):1076–1085, 2012. doi:10.1109/TMI.2012.2185247.

[18] J. J. Konkle, P. W. Goodwill, O. M. Carrasco-Zevallos, and S. M. Conolly. Projection Reconstruction Magnetic Particle Imaging. *IEEE Trans. Med. Imag.*, 32(2):338–347, 2012. doi:10.1109/TMI.2012.2227121.

[19] P. Elleaume, O. Chubar, and J. Chavanne. Computing 3D magnetic fields from insertion devices. In *Particle Accelerator Conference*, 1997. doi:10.1109/PAC.1997.753258.